

Article

An Improved Postprocessing Method to Mitigate the Macroscopic Cross-Slice B_0 Field Effect on R_2^* Measurements in the Mouse Brain at 7T

Chu-Yu Lee ¹, Daniel R. Thedens ¹, Olivia Lullmann ^{2,3}, Emily J. Steinbach ³, Michelle R. Tamplin ^{4,5,6} , Michael S. Petronek ⁵, Isabella M. Grumbach ^{4,5,6}, Bryan G. Allen ⁵, Lyndsay A. Harshman ³ and Vincent A. Magnotta ^{1,7,8,*} 

- ¹ Department of Radiology, University of Iowa, Iowa City, IA 52242, USA; chu-yu-lee@uiowa.edu (C.-Y.L.); dan-thedens@uiowa.edu (D.R.T.)
- ² Medical Scientist Training Program, University of Cincinnati College of Medicine, Cincinnati, OH 45267, USA; lullmaoa@mail.uc.edu
- ³ Stead Family Department of Pediatrics, Division of Pediatric Nephrology, University of Iowa Carver College of Medicine, Iowa City, IA 52242, USA; emily-steinbach@uiowa.edu (E.J.S.); lyndsay-harshman@uiowa.edu (L.A.H.)
- ⁴ Division of Cardiovascular Medicine, Abboud Cardiovascular Research Center, Department of Internal Medicine, University of Iowa Carver College of Medicine, Iowa City, IA 52242, USA; michelle-tamplin@uiowa.edu (M.R.T.); isabella-grumbach@uiowa.edu (I.M.G.)
- ⁵ Department of Radiation Oncology, Free Radical and Radiation Biology, University of Iowa Carver College of Medicine, Iowa City, IA 52242, USA; michael-petronek@uiowa.edu (M.S.P.); bryan-allen@uiowa.edu (B.G.A.)
- ⁶ Iowa City VA Center for the Prevention and Treatment of Visual Loss, Iowa City, IA 52246, USA
- ⁷ Department of Psychiatry, University of Iowa, Iowa City, IA 52242, USA
- ⁸ Department of Biomedical Engineering, University of Iowa, Iowa City, IA 52242, USA
- * Correspondence: vincent-magnotta@uiowa.edu; Tel.: +1-319-335-5482



Citation: Lee, C.-Y.; Thedens, D.R.; Lullmann, O.; Steinbach, E.J.; Tamplin, M.R.; Petronek, M.S.; Grumbach, I.M.; Allen, B.G.; Harshman, L.A.; Magnotta, V.A. An Improved Postprocessing Method to Mitigate the Macroscopic Cross-Slice B_0 Field Effect on R_2^* Measurements in the Mouse Brain at 7T. *Tomography* **2024**, *10*, 1074–1088. <https://doi.org/10.3390/tomography10070081>

Academic Editor: Emilio Quaia

Received: 1 May 2024

Revised: 27 June 2024

Accepted: 5 July 2024

Published: 11 July 2024



Copyright: © 2024 by the authors. Licensee MDPI, Basel, Switzerland. This article is an open access article distributed under the terms and conditions of the Creative Commons Attribution (CC BY) license (<https://creativecommons.org/licenses/by/4.0/>).

Abstract: The MR transverse relaxation rate, R_2^* , has been widely used to detect iron and myelin content in tissue. However, it is also sensitive to macroscopic B_0 inhomogeneities. One approach to correct for the B_0 effect is to fit gradient-echo signals with the three-parameter model, a sinc function-weighted monoexponential decay. However, such three-parameter models are subject to increased noise sensitivity. To address this issue, this study presents a two-stage fitting procedure based on the three-parameter model to mitigate the B_0 effect and reduce the noise sensitivity of R_2^* measurement in the mouse brain at 7T. MRI scans were performed on eight healthy mice. The gradient-echo signals were fitted with the two-stage fitting procedure to generate $R_{2corr_t}^*$. The signals were also fitted with the monoexponential and three-parameter models to generate $R_{2nocorr}^*$ and R_{2corr}^* , respectively. Regions of interest (ROIs), including the corpus callosum, internal capsule, somatosensory cortex, caudo-putamen, thalamus, and lateral ventricle, were selected to evaluate the within-ROI mean and standard deviation (SD) of the R_2^* measurements. The results showed that the Akaike information criterion of the monoexponential model was significantly reduced by using the three-parameter model in the selected ROIs ($p = 0.0039$ – 0.0078). However, the within-ROI SD of R_{2corr}^* using the three-parameter model was significantly higher than that of the $R_{2nocorr}^*$ in the internal capsule, caudo-putamen, and thalamus regions ($p = 0.0039$), a consequence partially due to the increased noise sensitivity of the three-parameter model. With the two-stage fitting procedure, the within-ROI SD of R_{2corr}^* was significantly reduced by 7.7–30.2% in all ROIs, except for the somatosensory cortex region with a fast in-plane variation of the B_0 gradient field ($p = 0.0039$ – 0.0078). These results support the utilization of the two-stage fitting procedure to mitigate the B_0 effect and reduce noise sensitivity for R_2^* measurement in the mouse brain.

Keywords: background gradients; R_2^* ; T_2^* ; post-processing; noise; gradient-echo; B_0 inhomogeneity; brain; myelin; iron; quantitative MRI

1. Introduction

The voxel-wise MR transverse relaxation rate, R_2^* , is sensitive to in vivo iron and myelin levels in the brain [1–3]. It has been used broadly to study brain development and neurodegenerative diseases in humans and mouse models associated with alternations in myelin and iron content [4–11]. R_2^* mapping is typically achieved by acquiring multi-echo gradient echo (GRE) images, followed by voxel-wise mono-exponential fitting of the signal decay. In the presence of iron and myelin, the magnetic susceptibility variations induce microscopic and mesoscopic field inhomogeneities in a voxel, resulting in accelerated signal decay and an increase in R_2^* . However, due to macroscopic voxel sizes, R_2^* values become inaccurate due to macroscopic field inhomogeneities (ΔB_0), such as regions near air-tissue interfaces. This considerable ΔB_0 effect leads to additional signal decay and overestimation of the R_2^* [12]. Therefore, correcting for the ΔB_0 effect is necessary for accurate R_2^* measurement.

The ΔB_0 effect can be mitigated by using a small voxel size on a microscopic or mesoscopic scale, but it is impractical due to the low signal-to-noise ratio (SNR) [12,13]. For GRE images with a high in-plane resolution but thicker slices such as in a typical two-dimensional (2D) acquisition, the ΔB_0 effect is predominant along the z-direction [12,14]. Many methods have been proposed to correct for the z-direction ΔB_0 effect on R_2^* measurement [14–25]. By assuming that the z-direction ΔB_0 is linear, the correction can be performed using one of the following methods: (1) adding a z-direction gradient to compensate for ΔB_0 [14,23]; (2) combining images from multiple acquisitions with incremental z-direction gradients [15,24,25]; or (3) applying a tailored RF excitation pulse [26] to reduce the intra-voxel spin dephasing due to ΔB_0 . Alternatively, the correction can be performed through postprocessing [16–22], which does not require pulse sequence modifications and can be generally applied to multi-echo GRE images. For an ideal slice profile and a linear ΔB_0 , the ΔB_0 effect on the measured R_2^* can be corrected by applying a sinc weighting function to the monoexponential model [17]. The corrected R_2^* (R_{2corr}^*) can be obtained by fitting the signal decay to the model with three parameters (S_0 , R_{2corr}^* and ΔB_0), referred to as the three-parameter model herein. Nonetheless, with an additional parameter (ΔB_0), the three-parameter model becomes more sensitive to noise at low SNR [17], particularly when the number of echo images is small. An initial estimate of ΔB_0 based on phase images [19–22] or a separate data acquisition [18] has been used to improve the R_{2corr}^* estimate, but this requires additional processing of phase images and may increase the scan time.

The purpose of this study is to present an improved postprocessing method to estimate the R_2^* in the mouse brain at 7T, which mitigates the cross-slice ΔB_0 effect while reducing sensitivity to noise. Based on the three-parameter model and an assumption of the smoothness of the ΔB_0 map, this study presents a two-stage fitting procedure to generate a less noisy estimate of R_2^* . The assumption of the smoothness of the B_0 and ΔB_0 maps has been utilized previously to reduce the noise effect on the ΔB_0 map for the R_2^* correction in the human brain and liver [21,22]. The novelty of the presented two-stage fitting procedure is that the ΔB_0 map is directly measured by fitting the magnitude images of the mouse brain, followed by the application of a smoothing filter to reduce the noise effects on the measured ΔB_0 map. By eliminating the need to process phase images, our method may help simplify the image processing workflow and provide more flexibility when phase images are unavailable or when obtaining an accurate estimate of B_0 maps through phase images is challenging. We demonstrate the feasibility of the presented method using in vivo mouse experiments and simulations.

2. Materials and Methods

2.1. In Vivo R_2^* Measurements

MRI scans were performed following the protocol approved by the Institutional Animal Care and Use Committees (IACUC) at the University of Iowa (IACUC Protocol #2112263). A total of 8 healthy mice (1 female and 7 males; 2–6 months of age) were imaged on a 7 Tesla Discovery MR901 system (GE Healthcare, Milwaukee, WI, USA) using a body

transmit coil and a 2-channel mouse brain receiver coil. The animals were sedated with isoflurane during the session. The imaging protocol included a vendor-supplied high-order B_0 shimming routine, followed by a FIESTA sequence for anatomical T_2 -weighted images (in-plane resolution of $104 \mu\text{m}^2$, slice thickness = $160 \mu\text{m}$, pixel bandwidth = 326 Hz , flip angle = 30° , TE/TR = $3/6.1 \text{ ms}$, number of averages = 4 , and scan time of 9 min and 28 s) and a 2D multi-echo GRE sequence for the R_2^* measurements (in-plane resolution of $156 \mu\text{m}^2$, slice thickness = $500 \mu\text{m}$, 18 axial slices, pixel bandwidth = 244 Hz , flip angle = 60° , TR = 1000 ms , 6 TEs of $2.5\text{--}22.5 \text{ ms}$ in increments of 4 ms , number of averages = 2 , and scan time of 4 min and 24 s).

2.2. Data Fitting

Data fitting was performed on the magnitude images in DICOM format that were reconstructed using a vendor-supplied image reconstruction routine. The reconstructed images had an image voxel size of $78 \times 78 \times 500 \mu\text{m}^3$.

Voxel-wise fitting was performed using the proposed two-stage fitting procedure as described below:

In the first stage of fitting, the signals in each image voxel of six-echo GRE images were fitted with the three-parameter model [17]:

$$S(\text{TE}) = S_0 \cdot e^{-R_{2\text{corr}}^* \text{TE}} \cdot \text{sinc}\left(\frac{\gamma \Delta B_0 \text{TE}}{2}\right) \quad (1)$$

where TE is the echo time of GRE images, S_0 is the signal at TE = 0, γ is the gyromagnetic ratio, and $\Delta B_0 = G_z \cdot z_0$ (G_z is the constant z-direction gradient and z_0 is the slice thickness). Due to the additional parameter (ΔB_0), the three-parameter model was sensitive to noise and generated noisy estimates of $\gamma \Delta B_0$ and $R_{2\text{corr}}^*$. By assuming that the $\gamma \Delta B_0$ is slowly varying on the x-y plane, a 2D Gaussian filter with a standard deviation (σ_{gaussian}) of $390 \mu\text{m}$, which was the length of five image pixels and around 2.5 times the in-plane image resolution, was applied to the $\gamma \Delta B_0$ map to reduce the effect of noise and generate a smoothed $\gamma \Delta B_0$ map ($\gamma \Delta B_{0\text{smooth}}$).

In the second stage of fitting, given the $\gamma \Delta B_{0\text{smooth}}$ map, the multi-echo GRE signals of each image voxel were divided by the sinc weighting function ($\text{sinc}(\gamma \Delta B_{0\text{smooth}} \text{TE}/2)$) in Equation (1) to remove the ΔB_0 effect. Following the division, the signals were fitted by the monoexponential model to obtain the $R_{2\text{corr}_f}^*$ with a reduced sensitivity to noise.

For comparison, the monoexponential models were also fitted to the six-echo GRE signals to generate the R_2^* map without correction ($R_{2\text{nocorr}}^*$). All of the fittings were performed using the trust-region-reflective algorithm [27] in Matlab R2023b (Mathworks, Inc.). The upper bound of $\gamma \Delta B_0$ was set to 88 Hz given the longest echo time of 22.5 ms [17]. The upper bound of R_2^* was set to 100 Hz .

Goodness-of-fit was evaluated using the reduced chi-square statistic (χ_v^2) [28]. χ_v^2 quantifies the sum of squares of the residuals normalized by the degrees of freedom of the model and the noise variance of the GRE images. A 95% confidence interval was defined as $\chi_v^2 < 2.4$ for a two-parameter model (the monoexponential model) and as $\chi_v^2 < 2.6$ for a three-parameter model. The Akaike information criterion (AIC) [29] was also used to compare the relative goodness-of-fit between the different fitting methods.

2.3. Regions of Interest Analysis

The regions of interest (ROIs), including the corpus callosum, internal capsule, somatosensory cortex, caudo-putamen, thalamus, and lateral ventricle, were selected to evaluate the R_2^* measurements. The ROIs were extracted from the structural labels of the P56 Mouse Brain atlas images [30–32]. These structural labels were brought into the individual GRE image space using a non-linear co-registration between the P56 Mouse Brain atlas images and individual anatomical T_2 -weighted images, followed by the linear co-registration between the individual anatomical T_2 -weighted images and the GRE images. All of the image co-registrations were performed using ANTs [32]. The ROIs on the GRE

images were visually examined and adjusted for each mouse and were applied to the R_2^* maps. The within-ROI mean and standard deviation (SD) values of the R_2^* measurements were computed for each ROI. The image voxels with a poor fitting (χ^2_v values outside the 95% confidence interval) were excluded from the ROI analysis.

2.4. Effect of the Smoothing Kernel Size

To investigate the effect of the smoothing kernel (σ_{gaussian}) of the 2D Gaussian filter applied to the $\gamma\Delta B_0$ map, four different values of the σ_{gaussian} , 234, 390, 546, and 702 μm , were used to smooth the $\gamma\Delta B_0$ map for the two-stage fitting procedure. The effect of the different smoothing kernels on $R_{2\text{corr}_t}^*$ was evaluated.

2.5. Statistics

Statistical analysis was performed to study (1) whether the fitting error, quantified by the AIC, of the monoexponential model is reduced by the application of the three-parameter model and two-stage fitting procedure; (2) whether the within-ROI SD of $R_{2\text{corr}}^*$ using the three-parameter model is higher than that of the $R_{2\text{nocorr}}^*$ of the monoexponential model due to the increased sensitivity to noise; and (3) whether the within-ROI SD of the $R_{2\text{corr}}^*$ is reduced by the application of the two-stage fitting procedure.

To address the above three questions, the one-tailed Wilcoxon signed-rank test was used for the comparisons, resulting in a total of 24 comparisons within the six ROIs. The significance level was adjusted for multiple comparisons using the false discovery rate [33]; p -value < 0.0078.

2.6. Simulations

To study the noise effects on the R_2^* measurements in the presence of a cross-slice ΔB_0 effect, representative in vivo multi-echo GRE signals were simulated using Equation (1) with the parameters R_2^* of 30 Hz, 6 TEs of 2.5–22.5 ms in increments of 4 ms, and S_0 of 50. $\gamma\Delta B_0$ was increased from 1 to 45 Hz to reflect the range of measured $\gamma\Delta B_0$ in the selected ROIs of the in vivo mouse brain. Rician noise was added to the signals with an SNR of 50, the average measured SNR of the in vivo mouse brain's 1st echo image. The procedure was repeated 1000 times to generate 1000 sets of noisy signals. One thousand sets of simulated noisy signals were fitted with the two-stage fitting procedure, monoexponential model, and three-parameter model as described in the Section 2.2. For the two-stage fitting procedure, 1000 measurements of $\gamma\Delta B_0$ were obtained through three-parameter model fitting and were smoothed to generate the $\gamma\Delta B_{0\text{smooth}}$ using a 1D Gaussian filter. The σ_{gaussian} of the 1D Gaussian filter was set to 25 data points to match the square kernel σ_{gaussian} (5×5 image pixels) used for the 2D Gaussian filter. Given the true values of R_2^* and $\gamma\Delta B_0$, the accuracies of the measured R_2^* and $\gamma\Delta B_0$ were evaluated using the root mean square error (RMSE). Moreover, the effect of the SNR on the R_2^* measurements was investigated by changing the SNR of the simulated signals from 20 to 100 and evaluating the accuracies of the measured R_2^* and $\gamma\Delta B_0$ at different SNR levels.

3. Results

Figure 1 illustrates the workflow of the presented two-stage fitting procedure. The $\gamma\Delta B_0$ map generated by the three-parameter fit showed a large ΔB_0 in regions with large magnetic susceptibility changes, such as the olfactory bulb, entorhinal cortex, and cerebellum, but it was noisy (Figure 1c). A smoothing kernel was applied to the $\gamma\Delta B_0$ map to reduce the noise effects while maintaining the spatial variation of ΔB_0 (Figure 1d). The $\gamma\Delta B_{0\text{smooth}}$ map was applied to the three-parameter model to remove the ΔB_0 effect from the signal and reduce the unknown parameters from three to two, thereby generating a less noisy $R_{2\text{corr}_t}^*$ map (Figure 1e).

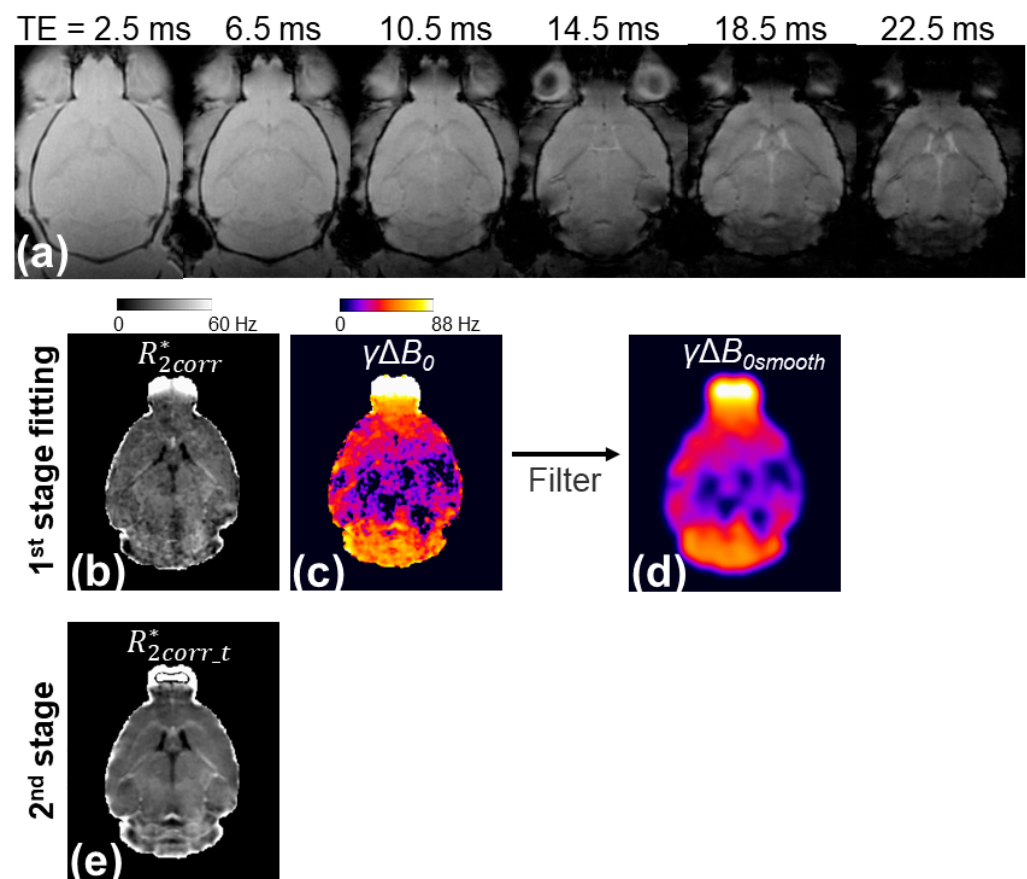


Figure 1. Illustration of the two-stage fitting procedure. In the first stage of fitting, the voxel-wise multi-echo GRE signals shown in (a) were fitted with the three-parameter model (Equation (1)) to generate corrected R_2^* (R_{2corr}^*) (b) and $\gamma\Delta B_0$ maps (c). Based on the assumption that the $\gamma\Delta B_0$ map is smooth on the x-y plane, a 2D Gaussian filter with a σ_{gaussian} of 390 μm was applied to the $\gamma\Delta B_0$ map to generate $\gamma\Delta B_{0smooth}$ (d). In the second stage of fitting, the multi-echo GRE signals of each image voxel were divided by the $\text{sinc}(\gamma\Delta B_{0smooth}TE/2)$ and were then fit with the monoexponential model to generate the $R_{2corr,t}^*$ map with reduced sensitivity to noise (e).

Figure 2 shows the computed $R_{2nocorr}^*$, R_{2corr}^* , and $R_{2corr,t}^*$ maps of three mice using the monoexponential model, three-parameter model, and two-stage fitting procedure. Figure 3 shows the corresponding χ^2_v maps using the three fitting methods. $R_{2nocorr}^*$ showed the ΔB_0 -induced increases in the regions near air–tissue interfaces, where fitting residuals of the monoexponential fit were elevated. These ΔB_0 effects were consistently mitigated on the R_{2corr}^* and $R_{2corr,t}^*$ maps. Furthermore, the noise effect on the R_{2corr}^* maps was mitigated on the $R_{2corr,t}^*$ maps without compromising the contrast of the brain structure.

Further quantitative analysis on the six selected ROIs was achieved through an image co-registration workflow, as shown in Figure 4. The AIC values of the monoexponential model were significantly reduced by using the three-parameter model and two-stage fitting procedure in all of the selected ROIs ($p = 0.0039\text{--}0.0078$) (Figure 5), suggesting that both the three-parameter model and two-stage fitting procedure are preferred to the monoexponential model in describing the data of the six ROIs.

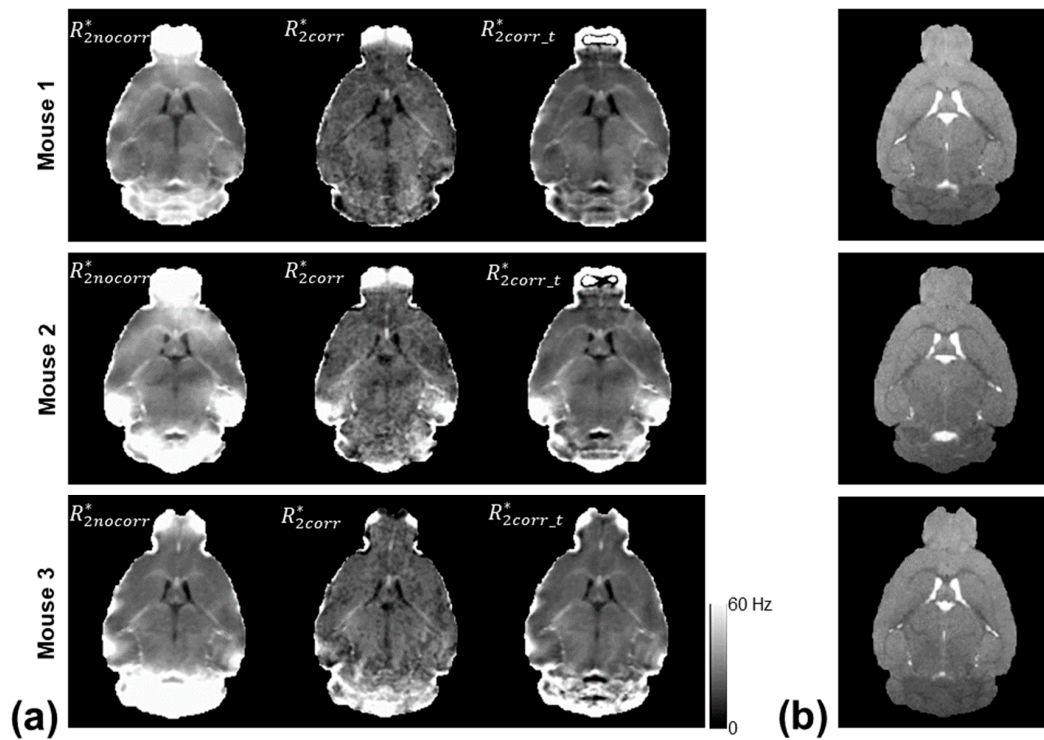


Figure 2. (a) Representative R_2^* measurements of three mice using the monoexponential model ($R_{2nocorr}^*$), three-parameter model (R_{2corr}^*), and two-stage fitting procedure ($R_{2corr_t}^*$), respectively, along with the anatomical T₂-weighted images (b) as a reference.

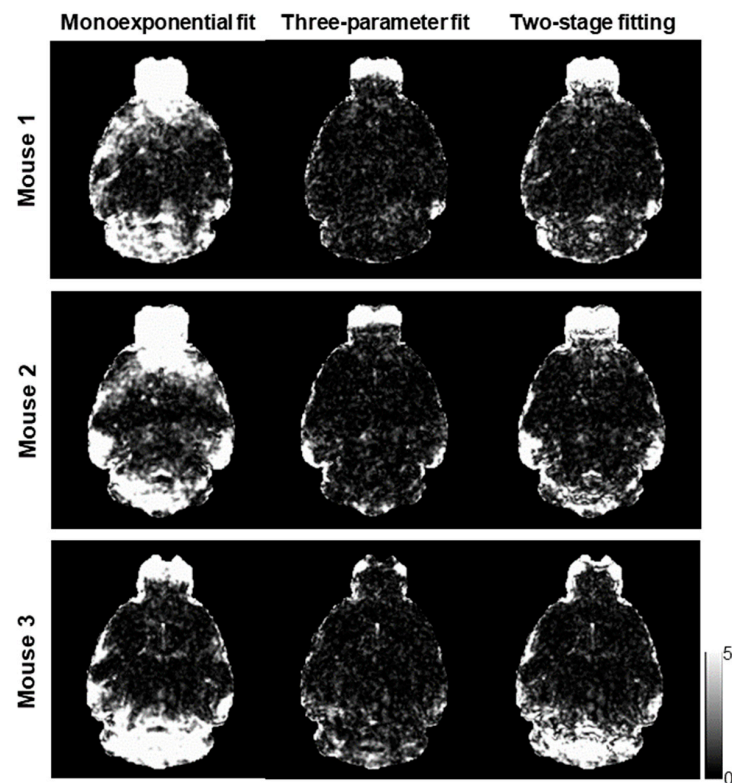


Figure 3. χ_v^2 maps corresponding to the voxel-wise fittings using the monoexponential model, three-parameter model, and two-stage fitting procedure, respectively, to generate the R_2^* measurements as shown in Figure 2.

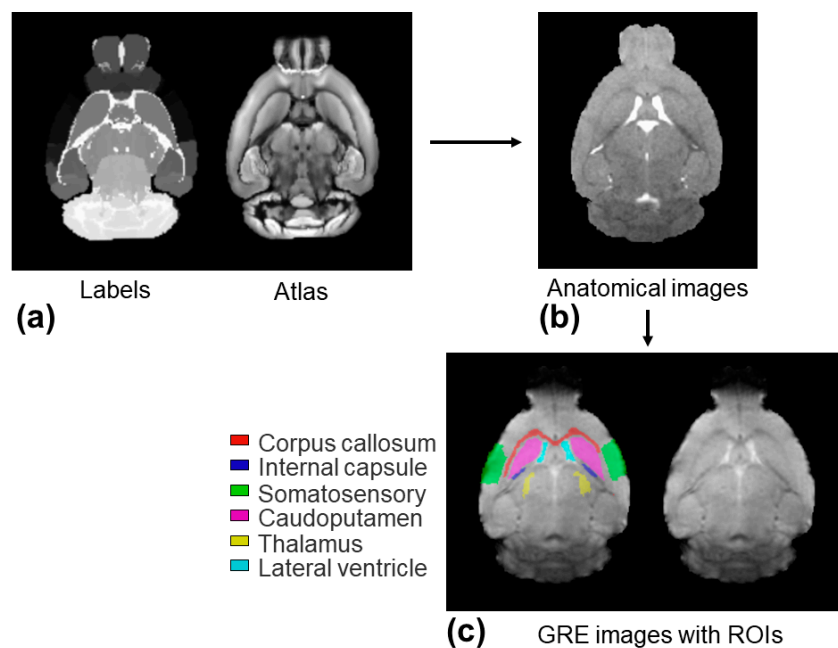


Figure 4. Illustration of the workflow of image co-registrations for the ROI analysis. Firstly, structural labels and the P56 Mouse Brain atlas images shown in (a) were brought into the space of individual anatomical images shown in (b) through a non-linear co-registration. Secondly, they were brought into the space of individual GRE images through a linear co-registration. (c) The selected six ROIs extracted from the structural labels on the individual GRE image space. ROIs were manually adjusted before they were applied to the R_2^* maps for quantification analysis.

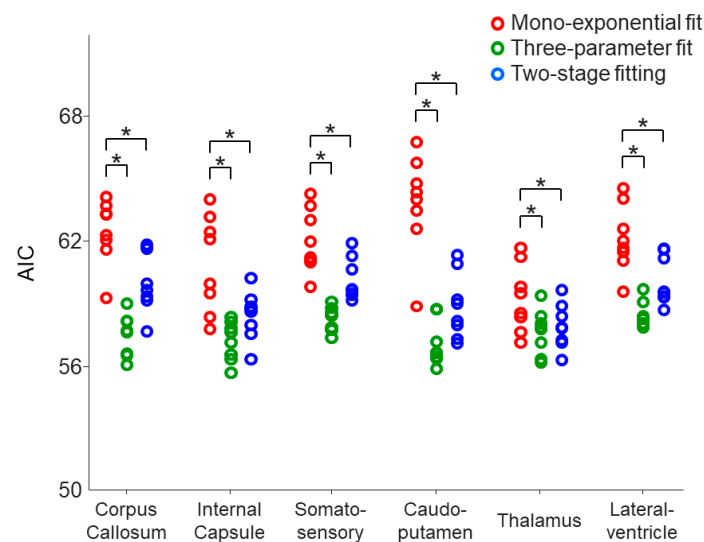


Figure 5. Comparison of the within-ROI mean AIC values on the eight mice using the monoexponential model, three-parameter model, and two-stage fitting procedure. * indicates that the AIC of the monoexponential model was significantly higher than that of the three-parameter model or two-stage fitting procedure. The comparisons were evaluated using the one-tailed Wilcoxon signed rank test ($p < 0.0078$).

The averaged inter-subject SD of the mean $R_{2nocorr}^*$ across the ROIs was decreased from 2.7 Hz to 1.4 and 1.5 Hz by using the three-parameter model and two-stage fitting procedure, respectively (Figure 6a). Nonetheless, the within-ROI SD of the R_{2corr}^* using the three-parameter model was significantly higher than that of the $R_{2nocorr}^*$ of the monoexponential model in the internal capsule, caudo-putamen, and thalamus regions

($p = 0.0039$) (Figure 6b). The higher within-ROI SD of the R_{2corr}^* was partially contributed by the increased noise sensitivity due to over-fitting. With the two-stage fitting procedure, the within-ROI SD of the R_{2corr}^* was significantly reduced by 7.7–30.2% in all the ROIs, except for the somatosensory cortex region ($p = 0.0039$ – 0.0078) (Figure 6b).

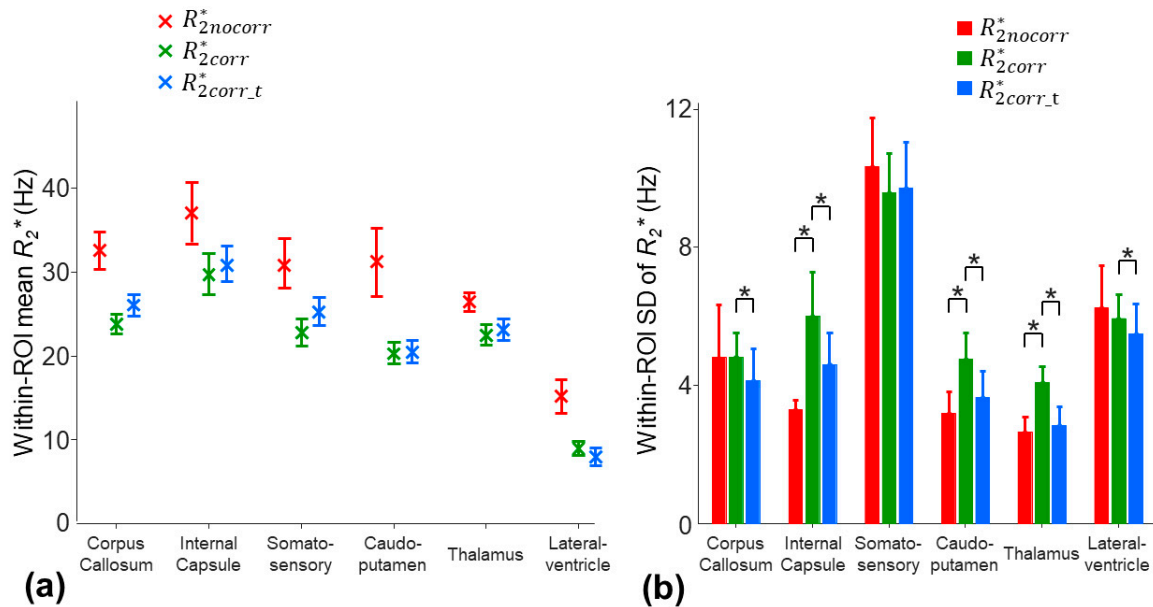


Figure 6. Comparison of the within-ROI mean (a) and SD (b) values of the R_2^* measurements on the eight mice using the monoexponential model ($R_{2nocorr}^*$), three-parameter model (R_{2corr}^*), and two-stage fitting procedure ($R_{2corr_t}^*$). * in (b) indicates that the SD of the R_{2corr}^* was significantly higher than that of the $R_{2nocorr}^*$ or $R_{2corr_t}^*$. The comparisons were evaluated using the one-tailed Wilcoxon signed-rank test ($p < 0.0078$).

For the two-stage fitting procedure, the application of different smoothing kernels to the $\gamma\Delta B_0$ map is illustrated in Figure 7.

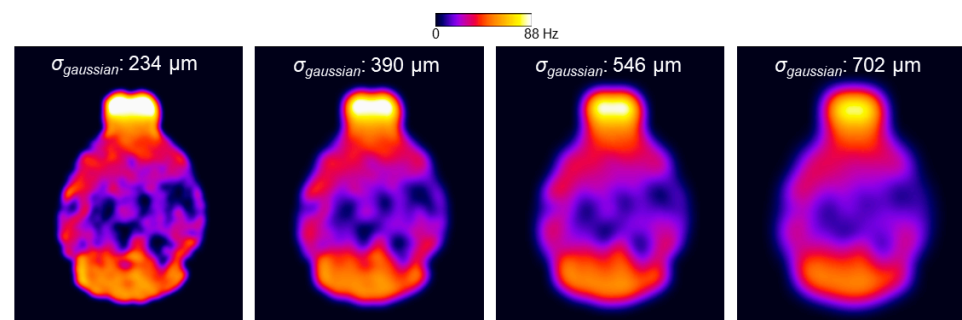


Figure 7. Illustration of the $\gamma\Delta B_{0smooth}$ map for the two-stage fitting procedure using different smoothing kernels (the $\sigma_{gaussian}$: 234, 390, 546, and 702 μm).

The application of a larger smoothing kernel ($\sigma_{gaussian}$ increased from 234 to 702 μm) led to decreases in the within-ROI SD of the $\gamma\Delta B_0$ in all the ROIs (Figure 8b). Among the selected ROIs, the smoothing procedure had the largest impact on the mean $\gamma\Delta B_0$ in the somatosensory region. The mean $\gamma\Delta B_0$ was decreased by 6.5 Hz in the somatosensory region, whereas the changes in the mean $\gamma\Delta B_0$ were less than 2.7 Hz in other ROIs (Figure 8a). This potential underestimate of the $\gamma\Delta B_0$ in the somatosensory cortex region using a larger smoothing kernel resulted in an increased mean $R_{2corr_t}^*$ by 11.4% (Figure 9a). In other ROIs, the changes in the mean $R_{2corr_t}^*$ were less than 5%. On the other hand, a larger smoothing kernel led to the reduced noise sensitivity of the $R_{2corr_t}^*$. The within-ROI SD of

the $R_{2corr_t}^*$ was decreased by 12.3%, 5.6%, and 14% in the internal capsule, caudo-putamen, and thalamus regions, respectively (Figure 9b).

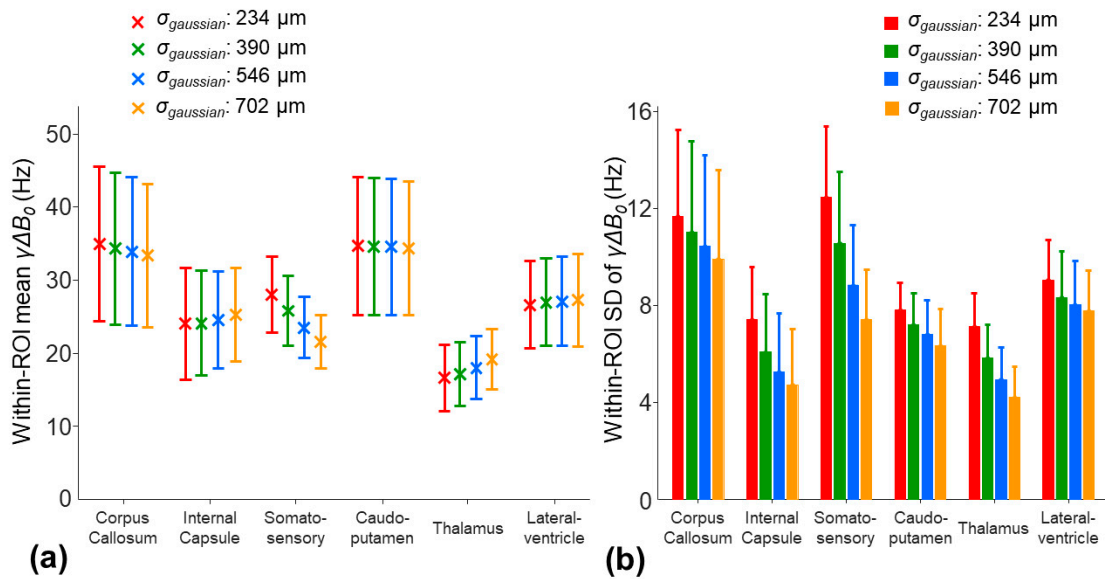


Figure 8. The effect of the different smoothing kernels (the $\sigma_{gaussian}$: 234, 390, 546, and 702 μm) on the within-ROI mean (a) and SD (b) values of the $\gamma\Delta B_{0smooth}$ map for the eight mice using the two-stage fitting procedure.

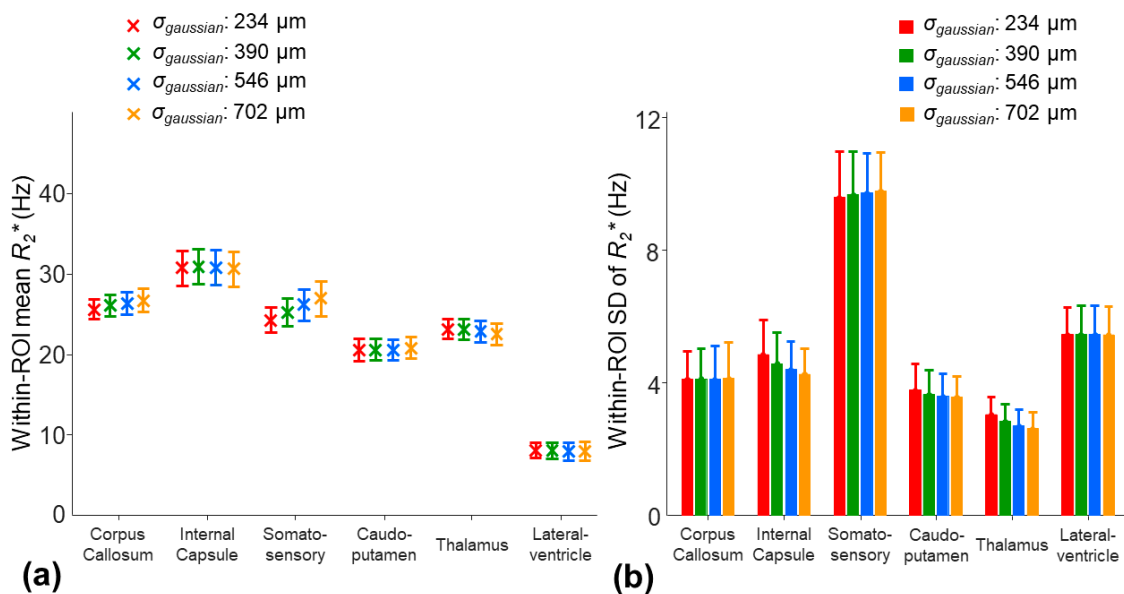


Figure 9. The effect of the different smoothing kernels (the $\sigma_{gaussian}$: 234, 390, 546, and 702 μm) on the within-ROI mean (a) and SD (b) values of the $R_{2corr_t}^*$ for the eight mice using the two-stage fitting procedure.

The simulations in the presence of a cross-slice ΔB_0 effect (true $\gamma\Delta B_0$ of 45 Hz) were performed to study the accuracies of the R_2^* and $\gamma\Delta B_0$ measurements. The $R_{2nocorr}^*$ had the highest RMSE of 19.3 Hz due to an overestimate of R_2^* (Figure 10a). The R_{2corr}^* showed an improved estimate of R_2^* (RMSE of 6.4 Hz) but had a high SD due to increased noise sensitivity; the mean \pm SD of R_{2corr}^* was 30.3 ± 6.5 Hz (Figure 10b). The $R_{2corr_t}^*$ was the most accurate (lowest RMSE of 2.4 Hz); the mean \pm SD of $R_{2corr_t}^*$ was 31 ± 2.4 Hz (Figure 10c). The $\gamma\Delta B_{0smooth}$ measured using the two-stage fitting procedure was more accurate than the $\gamma\Delta B_0$ measured using the three-parameter fit (RMSE: 1.1 Hz versus 6.3 Hz).

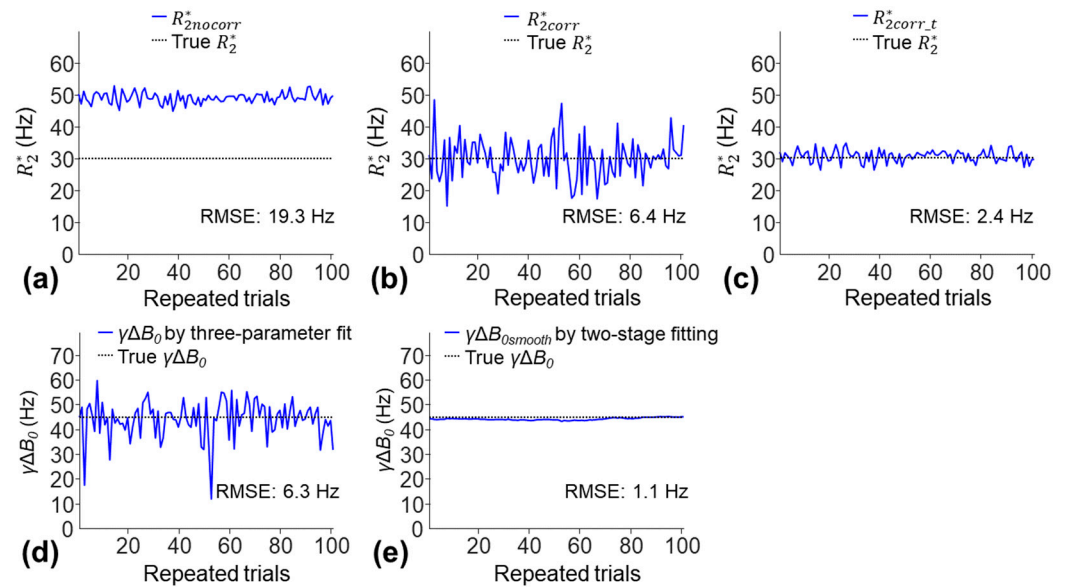


Figure 10. Illustration of the R_2^* (a–c) and $\gamma\Delta B_0$ (d,e) measurements using simulations with a cross-slice ΔB_0 effect. One-hundred sets of noisy signals were generated using the three-parameter model (Equation (1)) with an SNR of 50, R_2^* of 30 Hz, 6 TEs of 2.5–22.5 ms in increments of 4 ms, and $\gamma\Delta B_0$ of 45 Hz over 100 repeated trials. They were fitted with the monoexponential model, three-parameter model, and two-stage fitting procedure to generate the R_2^* measurements (a–c). The $\gamma\Delta B_0$ measurements in (d) were obtained through the three-parameter fit. They were smoothed by a 1D Gaussian filter with a $\sigma_{gaussian}$ of 25 data points to generate $\gamma\Delta B_{0smooth}$ (e) for the two-stage fitting procedure.

Further simulations were performed to study the accuracies of the R_2^* and $\gamma\Delta B_0$ measurements with a varied cross-slice ΔB_0 effect (true $\gamma\Delta B_0$ increased from 1 to 45 Hz). The $R_{2nocorr}^*$ became inaccurate with an increasing ΔB_0 effect (RMSE change: 1.6–19.3 Hz), whereas the accuracies of R_{2corr}^* and $R_{2corr,t}^*$ were more consistent (RMSE changes: 4.6–6.4 Hz and 1.7–2.6 Hz) (Figure 11a). The $R_{2corr,t}^*$ was more accurate than R_{2corr}^* and was nearly as accurate as $R_{2nocorr}^*$ when the ΔB_0 effect was small (true $\gamma\Delta B_0 < 10$ Hz). The $\gamma\Delta B_{0smooth}$ measured by the two-stage fitting procedure was more accurate than the $\gamma\Delta B_0$ measured by the three-parameter fit (Figure 11b). The accuracy of the $\gamma\Delta B_{0smooth}$ decreased when the ΔB_0 effect was small (true $\gamma\Delta B_0 < 10$ Hz), but this had little impact on the accuracy of $R_{2corr,t}^*$.

Simulations were also performed to study the dependence of the accuracies of the R_2^* and $\gamma\Delta B_0$ measurements on the SNR. With a true $\gamma\Delta B_0$ set to 45 Hz, the RMSE of the $R_{2nocorr}^*$ was mainly contributed by the cross-slice ΔB_0 effect and showed a smaller dependence on the SNR levels; RMSE change: 19.3–19.7 Hz versus 3.2–14.1 Hz for R_{2corr}^* and 1.1–6.9 for $R_{2corr,t}^*$ (Figure 12a). Across the SNR levels, $R_{2corr,t}^*$ was more accurate than $R_{2nocorr}^*$ and R_{2corr}^* . The $\gamma\Delta B_{0smooth}$ measured using the two-stage fitting procedure was more accurate than the $\gamma\Delta B_0$ measured using the three-parameter fit (Figure 12b).

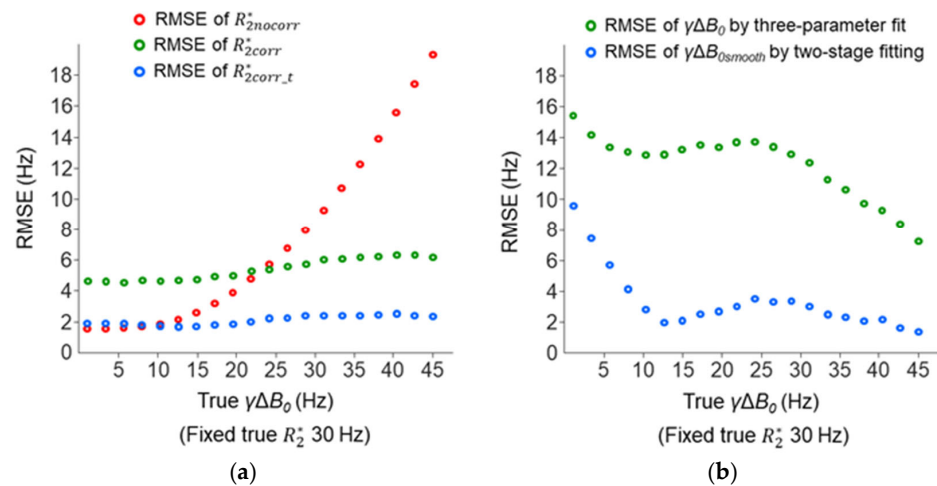


Figure 11. The RMSE of R_2^* (a) and $\gamma\Delta B_0$ (b) measurements across the different true $\gamma\Delta B_0$ values used in the simulations as described in Figure 10. Here, one thousand repeated trials were used to generate noisy signals to reduce the variability in the RMSE.

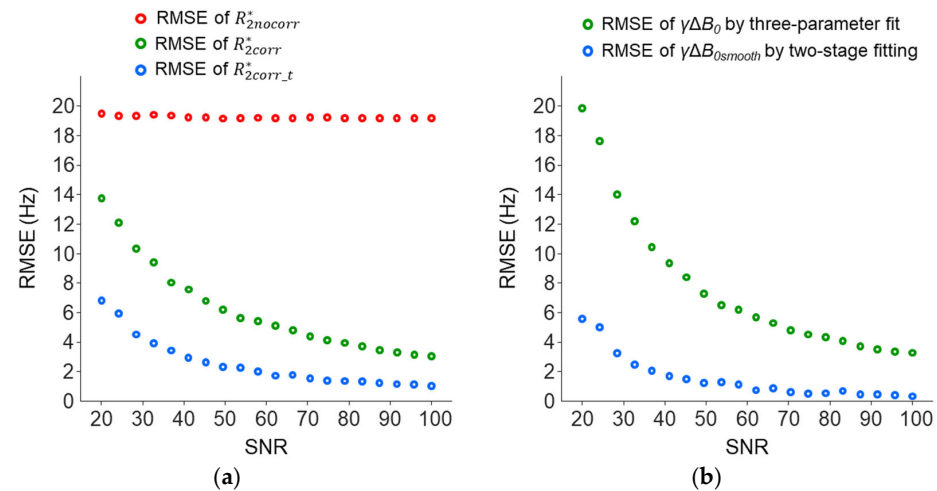


Figure 12. The RMSE of the R_2^* (a) and $\gamma\Delta B_0$ (b) measurements across the different SNRs used in the simulations with a true R_2^* of 30 Hz and true $\gamma\Delta B_0$ of 45 Hz as described in Figure 10. Here, one thousand repeated trials were used to generate noisy signals to reduce the variability in the RMSE.

4. Discussion

The ΔB_0 effects include a deviation of the GRE signal decay from the monoexponential model, a potential overestimate of the R_2^* , and increased inter-subject SD of R_2^* . With imaging data from eight mouse brains, we have shown that these ΔB_0 effects were effectively mitigated using the three-parameter model in the selected ROIs. We have further demonstrated that the noise-related within-ROI SD of $R_{2^{*}}^{corr}$ was significantly reduced by up to 30.2% using the two-stage fitting procedure. Moreover, simulations of R_2^* measurements in the presence of a cross-slice ΔB_0 effect and noise have demonstrated that $R_{2^{*}}^{corr_t}$ was more accurate than $R_{2^{*}}^{corr}$. Taken together, these results support the use of the two-stage fitting procedure to mitigate ΔB_0 effects and reduce noise sensitivity for R_2^* measurement in the mouse brain.

Applying a smoothing filter to the $\gamma\Delta B_0$ map for the two-stage fitting procedure assumes that the ΔB_0 is slowly varying on the x-y plane. Based on our results, this assumption may be valid in the selected corpus callosum, internal capsule, caudo-putamen, thalamus, and lateral ventricle regions of the mouse brain, where the application of the two-stage fitting procedure yields a significant reduction in the within-ROI SD of $R_{2^{*}}^{corr}$ by 7.7 to 30.2%. For the selected ROIs in the deep brain structure, including the internal capsule,

caudo-putamen, and thalamus regions, the within-ROI SD of the $R_{2corr_t}^*$ in these ROIs was further reduced with a larger smoothing kernel applied to the $\gamma\Delta B_0$ map. However, the assumption of a slow in-plane variation in $\gamma\Delta B_0$ is invalid in regions with a rapidly varying $\gamma\Delta B_0$ on the x-y plane, such as the somatosensory cortex region close to air-tissue interfaces and with large magnetic susceptibility changes. In these regions, the $\gamma\Delta B_0$ map as well as $R_{2corr_t}^*$ showed a strong dependence on the smoothing kernel. Furthermore, the application of a larger smoothing kernel only led to small changes (<2%) in the within-ROI SD of $R_{2corr_t}^*$, indicating no benefits of using a larger smoothing kernel in these regions. In the presence of a fast in-plane variation in $\gamma\Delta B_0$, applying a smoothing filter may lead to an underestimate of $\gamma\Delta B_0$ and an overestimate of $R_{2corr_t}^*$ [17]. This $R_{2corr_t}^*$ change may in turn increase the within-ROI SD of $R_{2corr_t}^*$ and offset the benefit of the two-stage fitting procedure to reduce noise sensitivity. Considering the tradeoff, this study used a smoothing kernel of 390 μm , around 2.5 times the in-plane image resolution, for the two-stage fitting procedure. Importantly, we observed only a moderate dependence of the mean $R_{2corr_t}^*$ on the smoothing kernel in the selected ROIs; the changes were less than 11.4%.

In our study, the $\gamma\Delta B_0$ map was measured through the fitting of the six echo magnitude images with the three-parameter model that assumes a linear ΔB_0 across a slice. The assumption of a linear ΔB_0 implies a slowly varying ΔB_0 across a slice and may be invalid in regions with a rapidly varying cross-slice ΔB_0 , such as a high ΔB_0 . In our study, regions with a measured $\gamma\Delta B_0$ larger than 60 Hz, such as the olfactory bulb, entorhinal cortex, and cerebellum, showed a potential overestimate of the R_{2corr}^* and thus an inaccurate estimate of the $\gamma\Delta B_0$ map using the three-parameter model (Figure 2). An alternative approach to measuring the $\gamma\Delta B_0$ map is using phase images [19–22]. The phase image-based approach typically requires phase unwrapping procedures and an assumption of a smoothed B_0 on the x-y plane to reliably measure the B_0 map. Thus, the phase-based approach remains limited in the presence of a rapidly varying ΔB_0 across a slice or at high fields with a fast phase evolution. Our study demonstrates the feasibility of measuring the $\gamma\Delta B_0$ map through the fitting to magnitude images, omitting the need for processing the phase images.

The use of magnitude images to measure the $\gamma\Delta B_0$ map relies on the sinc function-weighted signal decay, which is particularly pronounced at long echo times. When the ΔB_0 effect is small, e.g., $\gamma\Delta B_0 < 10$ Hz, the signal attenuation may be too small to reliably measure the $\gamma\Delta B_0$. As shown in our simulation, the accuracy of the $\gamma\Delta B_{0smooth}$ decreased when the true $\gamma\Delta B_0$ was less than 10 Hz. However, the inaccurate $\gamma\Delta B_{0smooth}$ had little impact on the accuracy of the $R_{2corr_t}^*$ in our simulation. When the ΔB_0 effect is small, the ΔB_0 effect on the signal attenuation may be indistinguishable from the noise, and the accuracy of the $\gamma\Delta B_{0smooth}$ becomes less relevant to the $R_{2corr_t}^*$. On the other hand, phase-based methods may be more sensitive to detecting ΔB_0 -induced phase changes even when the ΔB_0 effect is small. This may lead to more accurate estimates of $\gamma\Delta B_0$ and R_2^* .

In addition to the increased within-ROI SD of the R_2^* measurement, a low SNR could induce bias in R_2^* measurement. In regions with a rapidly varying cross-slice ΔB_0 , the sinc function-weighted signal decay is faster than the monoexponential decay at longer echo times, resulting in low SNR. In our study, the average SNR of the mouse brain's 1st echo image (TE = 2.5 ms) was around 50. Given a R_2^* of 30 Hz and the measured $\gamma\Delta B_0$ of 10–50 Hz in our selected ROIs, the SNR of the longest echo signal (TE = 22.5 ms) is around 15–27. However, the SNR at TE = 22.5 ms drops to 3–11 when the $\gamma\Delta B_0$ is increased to 60–80 Hz in the olfactory bulb, entorhinal cortex, and cerebellum regions. This $\gamma\Delta B_0$ -induced signal drop at longer echo times may affect the ability of the three-parameter model to characterize the signal decay, likely resulting in an underestimate of $\gamma\Delta B_0$ and an overestimate of R_{2corr}^* [17].

The presented two-stage fitting procedure is based on the three-parameter model; therefore, it remains subject to the limitations of the three-parameter model in the presence of a rapidly varying cross-slice ΔB_0 as described above. Considering these limitations, this study focused on the ROIs with a $\gamma\Delta B_0$ less than 50 Hz. To account for a rapidly varying cross-slice ΔB_0 , previous studies have used separate data acquisition for a 3D

high-resolution $\gamma\Delta B_0$ map [16,18] and a quadratic function to approximate the cross-slice ΔB_0 [16]. However, such approaches increase the scan time and require more fitting parameters to mitigate the ΔB_0 effect.

Our method shares some similarities with previous works by Dong et al. [34] and Tan et al. [35] in seeking the optimized solution for multiple parametric measurements that ensures data consistency and the smoothness of the phase maps. The major difference is that the previous works include the regularization of the loss function to ensure the smoothness of the phase maps, allowing one to address the optimization with more unknowns and more constraints. In contrast, our method ensures data consistency through the voxel-wise fitting, followed by applying a smoothing filter to smooth the phase maps. Solving regularized optimization normally requires multiple iterations and a longer computation time. Our method requires a short computation time but is limited to addressing a simple problem. Another difference is that the work by Tan et al. [35] involves joint image reconstruction and parametric measurements for optimization. This allows one to reconstruct the undersampled k-space data with potential benefits in shortening the scan time and reducing motion artifacts. By contrast, our method only performs parametric measurements on the magnitude images, which are reconstructed using a vendor-supplied image reconstruction routine. Therefore, our method does not require k-space data and can be generally applied to multi-echo GRE images retrospectively.

In this study, multi-echo GRE acquisition was performed using the axial orientation with 18 slices to cover the entire brain. Another common option for 2D acquisition is to use the coronal orientation. However, the axial orientation allows one to cover a larger area of the mouse brain in a 2D slice than the coronal orientation. This is beneficial to our proposed method due to a smaller proportion of an axial image being influenced by large magnetic susceptibility changes near the aural cavity or air–tissue interfaces. Therefore, the assumption of a slow in-plane variation in $\gamma\Delta B_0$ can be applicable to a larger region of the brain, allowing the smoothing filter to effectively reduce the noise effect on the $\gamma\Delta B_0$ map.

This study applied χ_v^2 and AIC to evaluate the goodness-of-fit. For each image voxel, the χ_v^2 was used to determine whether the individual model fits the data considering the noise and the degrees of freedom of the model. Following the exclusion of the image voxels with a poor fit, AIC was applied subsequently to compare the goodness-of-fit of the models within each ROI considering the complexity of the model. Either assessment can eliminate the possibility of over-fitting. Therefore, this study focused on whether the application of the three-parameter model or two-stage fitting procedure improves the monoexponential fit rather than finding the best model to fit the data.

5. Conclusions

The presented two-stage fitting procedure reduced the noise-related within-ROI SD of R_{2corr}^* in regions with a slow in-plane variation of $\gamma\Delta B_0$. This suggests that it can be used for the three-parameter model to mitigate the cross-slice ΔB_0 effects and reduce noise sensitivity for R_2^* measurement in the mouse brain. It utilizes fittings of the magnitude images without processing the phase images, thereby helping simplify the image processing workflow.

Author Contributions: Formal analysis, D.R.T., O.L., E.J.S., M.R.T., M.S.P., I.M.G., B.G.A. and L.A.H.; investigation, O.L., E.J.S., M.R.T., M.S.P., I.M.G., B.G.A. and L.A.H.; methodology, C.-Y.L., D.R.T. and V.A.M.; software, C.-Y.L. and V.A.M.; validation, C.-Y.L., D.R.T. and V.A.M.; writing—original draft, C.-Y.L.; writing—review and editing, D.R.T., O.L., E.J.S., M.R.T., M.S.P., I.M.G., B.G.A., L.A.H. and V.A.M. All authors have read and agreed to the published version of the manuscript.

Funding: We gratefully acknowledge support from the Stead Family Department of Pediatrics Research Grant Program, Children’s Miracle Network, and National Institute of Health grants P01CA217797 and R21CA270742. The MR imaging facility was supported in part by NIH Instrumentation grant S10OD034261.

Institutional Review Board Statement: The animal study protocol was approved by the Institutional Ethics Committee of the University of Iowa (protocol code 2112263 and date of approval: 1 November 2023).

Informed Consent Statement: Not applicable.

Data Availability Statement: Study data are available from the corresponding author upon request.

Conflicts of Interest: The authors declare no conflicts of interest.

References

1. Deistung, A.; Schäfer, A.; Schweser, F.; Biedermann, U.; Turner, R.; Reichenbach, J.R. Toward in vivo histology: A comparison of quantitative susceptibility mapping (QSM) with magnitude-, phase-, and R2*-imaging at ultra-high magnetic field strength. *Neuroimage* **2013**, *65*, 299–314. [[CrossRef](#)]
2. Shin, H.G.; Lee, J.; Yun, Y.H.; Yoo, S.H.; Jang, J.; Oh, S.H.; Nam, Y.; Jung, S.; Kim, S.; Fukunaga, M.; et al. χ -separation: Magnetic susceptibility source separation toward iron and myelin mapping in the brain. *Neuroimage* **2021**, *240*, 118371. [[CrossRef](#)]
3. Duyn, J.H.; Schenck, J. Contributions to magnetic susceptibility of brain tissue. *NMR Biomed.* **2017**, *30*, 3546. [[CrossRef](#)]
4. Antharam, V.; Collingwood, J.F.; Bullivant, J.P.; Davidson, M.R.; Chandra, S.; Mikhaylova, A.; Finnegan, M.E.; Batich, C.; Forder, J.R.; Dobson, J. High field magnetic resonance microscopy of the human hippocampus in Alzheimer's disease: Quantitative imaging and correlation with iron. *Neuroimage* **2012**, *59*, 1249–1260. [[CrossRef](#)]
5. Rossi, M.; Ruottinen, H.; Soimakallio, S.; Elovaara, I.; Dastidar, P. Clinical MRI for iron detection in Parkinson's disease. *Clin. Imaging* **2013**, *37*, 631–636. [[CrossRef](#)]
6. Kor, D.; Birkel, C.; Ropele, S.; Doucette, J.; Xu, T.; Wiggermann, V.; Hernández-Torres, E.; Hametner, S.; Rauscher, A. The role of iron and myelin in orientation dependent R(2)(*) of white matter. *NMR Biomed.* **2019**, *32*, e4092. [[CrossRef](#)]
7. Bagnato, F.; Hametner, S.; Boyd, E.; Endmayr, V.; Shi, Y.; Ikonomidou, V.; Chen, G.; Pawate, S.; Lassmann, H.; Smith, S.; et al. Untangling the R2* contrast in multiple sclerosis: A combined MRI-histology study at 7.0 Tesla. *PLoS ONE* **2018**, *13*, e0193839. [[CrossRef](#)]
8. Yatmark, P.; Huaijantug, S.; Teerapan, W.; Svasti, S.; Fucharoen, S.; Morales, N.P. MRI imaging and histopathological study of brain iron overload of β -thalassemic mice. *Magn. Reson. Imaging* **2019**, *61*, 267–272. [[CrossRef](#)]
9. Chang, S.K.; Kim, J.; Lee, D.; Yoo, C.H.; Jin, S.; Rhee, H.Y.; Ryu, C.W.; Lee, J.K.; Cho, H.; Jahng, G.H. Mapping of microvascular architecture in the brain of an Alzheimer's disease mouse model using MRI. *NMR Biomed.* **2021**, *34*, e4481. [[CrossRef](#)]
10. Wang, C.; Foxley, S.; Ansoorge, O.; Bangerter-Christensen, S.; Chiew, M.; Leonte, A.; Menke, R.A.; Mollink, J.; Pallegage-Gamarallage, M.; Turner, M.R.; et al. Methods for quantitative susceptibility and R2* mapping in whole post-mortem brains at 7T applied to amyotrophic lateral sclerosis. *Neuroimage* **2020**, *222*, 117216. [[CrossRef](#)]
11. Lee, J.; Shmueli, K.; Kang, B.T.; Yao, B.; Fukunaga, M.; van Gelderen, P.; Palumbo, S.; Bosetti, F.; Silva, A.C.; Duyn, J.H. The contribution of myelin to magnetic susceptibility-weighted contrasts in high-field MRI of the brain. *Neuroimage* **2012**, *59*, 3967–3975. [[CrossRef](#)] [[PubMed](#)]
12. Haacke, E.M.; Tkach, J.A.; Parrish, T.B. Reduction of T2* dephasing in gradient field-echo imaging. *Radiology* **1989**, *170*, 457–462. [[CrossRef](#)]
13. Reichenbach, J.R.; Venkatesan, R.; Yablonskiy, D.A.; Thompson, M.R.; Lai, S.; Haacke, E.M. Theory and application of static field inhomogeneity effects in gradient-echo imaging. *J. Magn. Reson. Imaging* **1997**, *7*, 266–279. [[CrossRef](#)]
14. Frahm, J.; Merboldt, K.D.; Hänicke, W. Direct FLASH MR imaging of magnetic field inhomogeneities by gradient compensation. *Magn. Reson. Med.* **1988**, *6*, 474–480. [[CrossRef](#)]
15. Yang, Q.X.; Williams, G.D.; Demeure, R.J.; Mosher, T.J.; Smith, M.B. Removal of local field gradient artifacts in T2*-weighted images at high fields by gradient-echo slice excitation profile imaging. *Magn. Reson. Med.* **1998**, *39*, 402–409. [[CrossRef](#)]
16. Yang, X.; Sammet, S.; Schmalbrock, P.; Knopp, M.V. Postprocessing correction for distortions in T2* decay caused by quadratic cross-slice B0 inhomogeneity. *Magn. Reson. Med.* **2010**, *63*, 1258–1268. [[CrossRef](#)]
17. Fernández-Seara, M.A.; Wehrli, F.W. Postprocessing technique to correct for background gradients in image-based R*(2) measurements. *Magn. Reson. Med.* **2000**, *44*, 358–366. [[CrossRef](#)] [[PubMed](#)]
18. An, H.; Lin, W. Cerebral oxygen extraction fraction and cerebral venous blood volume measurements using MRI: Effects of magnetic field variation. *Magn. Reson. Med.* **2002**, *47*, 958–966. [[CrossRef](#)]
19. Peters, A.M.; Brookes, M.J.; Hoogenraad, F.G.; Gowland, P.A.; Francis, S.T.; Morris, P.G.; Bowtell, R. T2* measurements in human brain at 1.5, 3 and 7 T. *Magn. Reson. Imaging* **2007**, *25*, 748–753. [[CrossRef](#)]
20. Dahnke, H.; Schaeffter, T. Limits of detection of SPIO at 3.0 T using T2 relaxometry. *Magn. Reson. Med.* **2005**, *53*, 1202–1206. [[CrossRef](#)]
21. Hernando, D.; Vigen, K.K.; Shimakawa, A.; Reeder, S.B. R*(2) mapping in the presence of macroscopic B0 field variations. *Magn. Reson. Med.* **2012**, *68*, 830–840. [[CrossRef](#)]
22. Volz, S.; Hattungen, E.; Preibisch, C.; Gasser, T.; Deichmann, R. Reduction of susceptibility-induced signal losses in multi-gradient-echo images: Application to improved visualization of the subthalamic nucleus. *Neuroimage* **2009**, *45*, 1135–1143. [[CrossRef](#)]
23. Soellradl, M.; Strasser, J.; Lesch, A.; Stollberger, R.; Ropele, S.; Langkammer, C. Adaptive slice-specific z-shimming for 2D spoiled gradient-echo sequences. *Magn. Reson. Med.* **2021**, *85*, 818–830. [[CrossRef](#)]
24. Wild, J.M.; Martin, W.R.; Allen, P.S. Multiple gradient echo sequence optimized for rapid, single-scan mapping of R(2)(*) at high B0. *Magn. Reson. Med.* **2002**, *48*, 867–876. [[CrossRef](#)]

25. Ordidge, R.J.; Gorell, J.M.; Deniau, J.C.; Knight, R.A.; Helpner, J.A. Assessment of relative brain iron concentrations using T2-weighted and T2*-weighted MRI at 3 Tesla. *Magn. Reson. Med.* **1994**, *32*, 335–341. [[CrossRef](#)]
26. Cho, Z.H.; Ro, Y.M. Reduction of susceptibility artifact in gradient-echo imaging. *Magn. Reson. Med.* **1992**, *23*, 193–200. [[CrossRef](#)]
27. Branch, M.A.; Coleman, T.F.; Li, Y. A Subspace, Interior, and Conjugate Gradient Method for Large-Scale Bound-Constrained Minimization Problems. *SIAM J. Sci. Comput.* **1999**, *21*, 1–23. [[CrossRef](#)]
28. Bevington, P.R.; Robinson, D.K. *Data Reduction and Error Analysis for the Physical Sciences*; McGraw-Hill: New York, NY, USA, 1992.
29. Akaike, H. Information theory and an extension of the maximum likelihood principle. In *Selected Papers of Hirotugu Akaike*; Springer: Berlin/Heidelberg, Germany, 1998; pp. 199–213.
30. Lein, E.S.; Hawrylycz, M.J.; Ao, N.; Ayres, M.; Bensinger, A.; Bernard, A.; Boe, A.F.; Boguski, M.S.; Brockway, K.S.; Byrnes, E.J.; et al. Genome-wide atlas of gene expression in the adult mouse brain. *Nature* **2007**, *445*, 168–176. [[CrossRef](#)]
31. Bakker, R.; Tiesinga, P.; Kötter, R. The Scalable Brain Atlas: Instant Web-Based Access to Public Brain Atlases and Related Content. *Neuroinformatics* **2015**, *13*, 353–366. [[CrossRef](#)]
32. Avants, B.B.; Tustison, N.J.; Song, G.; Cook, P.A.; Klein, A.; Gee, J.C. A reproducible evaluation of ANTs similarity metric performance in brain image registration. *Neuroimage* **2011**, *54*, 2033–2044. [[CrossRef](#)]
33. Benjamini, Y.; Hochberg, Y. Controlling the False Discovery Rate: A Practical and Powerful Approach to Multiple Testing. *J. R. Stat. Soc. Ser. B Methodol.* **1995**, *57*, 289–300. [[CrossRef](#)]
34. Dong, Y.; Koolstra, K.; Riedel, M.; van Osch, M.J.P.; Börnert, P. Regularized joint water-fat separation with B(0) map estimation in image space for 2D-navigated interleaved EPI based diffusion MRI. *Magn. Reson. Med.* **2021**, *86*, 3034–3051. [[CrossRef](#)]
35. Tan, Z.; Unterberg-Buchwald, C.; Blumenthal, M.; Scholand, N.; Schaten, P.; Holme, C.; Wang, X.; Raddatz, D.; Uecker, M. Free-Breathing Liver Fat, R₂* and B₀ Field Mapping Using Multi-Echo Radial FLASH and Regularized Model-Based Reconstruction. *IEEE Trans. Med. Imaging* **2023**, *42*, 1374–1387. [[CrossRef](#)]

Disclaimer/Publisher’s Note: The statements, opinions and data contained in all publications are solely those of the individual author(s) and contributor(s) and not of MDPI and/or the editor(s). MDPI and/or the editor(s) disclaim responsibility for any injury to people or property resulting from any ideas, methods, instructions or products referred to in the content.